Post mortem Study of Catalyst Degradations Occurring in High-Temperature Proton Exchange Membrane Fuel Cells Upon Start-Stop Operation

Axelle Baudy, Maël Durand, Francine Roussel-Dherbey, Grégory Berthomé, Nicolas Sergent, Christophe Turpin, Jérémi Regnier, Amine Jaafar, Laetitia Dubau, Marion Scohy, et al.

Post mortem Study of Catalyst Degradations Occurring in High-Temperature Proton Exchange Membrane Fuel Cells Upon Start-stop Operation

Axelle Baudy [1 2], Maël Durand [2], Francine Roussel-Dherbey [3], Grégory Berthomé [4], Nicolas Sergent [1], Christophe Turpin [5], Jérémi Regnier [5], Amine Jaafar [5], Laetitia Dubau [1], Marion Scohy[2] , Marian Chatenet [1]

[1] Univ. Grenoble Alpes, Univ. Savoie Mont Blanc, CNRS, Grenoble INP, Institute of Engineering and Management Univ. Grenoble Alpes, LEPMI, 38000, Grenoble, France

[2] Safran Power Units, 8 chemin du pont de Rupé 31200 Toulouse

[3] Univ. Grenoble Alpes, Grenoble Institute of Technologies, CMTC, 1260 rue de la Piscine, 38402, Saint-Martin d'Hères, France

[4] Grenoble Institute of Technologies – SIMaP, 1130 rue de la Piscine, 38402 Saint-Martin d'Hères, France

[5] LAPLACE, Université de Toulouse, CNRS, INPT, UPS, Toulouse, France

Keywords: HT-PEMFC, *post mortem* physicochemical and electrochemical characterizations, degradation mechanisms, electrocatalyst, PtNi/C, MEA, PBI

ABSTRACT

High-temperature proton exchange membrane fuel cells (HT-PEMFCs) could replace fossil fuel-based technologies for applications which cannot involve bulky/heavy cooling systems, such as aeronautics. However, severe materials degradations upon operation prevent performance retention for acceptable lifetimes. While works already reported degradations in HT-PEMFC, *post mortem* characterizations of used HT-PEMFC MEAs remain scarce. Herein, HT-PEMFC performance degradation is studied by applying a startup/shutdown protocol to a short-stack operated at 160°C; one of the MEA is characterized using complementary physicochemical/electrochemical techniques to identify/understand the degradation mechanisms and their origin. This start/stop operation mode (co-flow gas reactants) leads to substantial degradation inhomogeneity. For the anode, migration, coalescence and detachment of Pt nanoparticles are witnessed induced by high-surface-area carbon support functionalization and corrosion. The anode electrochemical surface area (ECSA) remains constant at the inlet and increases significantly at the outlet, following inhomogeneous degradation of the cathode catalyst: the Pt^{z+} ions formed at high potential/oxidizing conditions concentrate towards the outlet, where they redeposit locally or at the anode, after diffusion/migration across the PBI membrane. Hence, the cathode ECSA decreases significantly at the inlet. Furthermore, intense Ni-leaching from the initial PtNi alloy catalyst is reported as a result of O_2 mass-transport and phosphoric acid dilution inhomogeneity.

INTRODUCTION

In a context of decarbonation, hydrogen fuel cell systems are an interesting alternative to fossil fuel-based technologies, owing to their low CO_2 emissions (if H_2 is of renewable origin). Various types of polymer electrolyte membrane fuel cell are currently developed for a wide range of applications, based on low (<100°C) and high temperature (>100°C) proton exchange membranes (LT-PEMFC and HT-PEMFC). The main difference between the low and high temperature technologies is the nature of the electrolyte used for protons conduction. For LT-PEMFCs, the ionomer is usually a perfluorinated polymer, hydrated by liquid water. This polymer has a high proton conductivity below 100°C[1]. However, at higher temperature, water vapor cannot correctly hydrate the ionomer and ensure a significant proton conductivity. Besides, per- and polyfluoroalkyl substances (PFAS) are under intense focus in the USA, the European Union and France[2], and might be banned in a near-future, putting threat on the present technologies of LT-PEMFCs. On the contrary, HT-PEMFCs are not bothered by these biases: the most common polymer used as electrode separator and electrolyte for HT-PEMFC is acid-doped polybenzimidazole (PBI), a non-fluorinated compound; PBI exhibits high mechanical resistance properties and the phosphoric acid doping allows efficient proton conductivity above 100°C [1,3]. Hence, HT-PEMFC is a technology that offers various general advantages: the water management is easier, as it is not necessary to feed humidified gases, or even to maintain the membrane hydrated. In addition, the absence of humidification system combined to the operation at 160°C (allowing to downsize the cooling system) overall improves the system specific power/energy and provides higher resistance to CO poisoning [3].

However, the technology suffers from a real lack of maturity in terms of performances and durability. While high temperature should increase the anode and cathode reactions kinetic (a

positive effect), the poisoning effect of strongly adsorbed phosphate anions largely decreases the reactants (H_2 and O_2) interaction with the catalyst and negatively impacts the global performances of the two electrodes of the HT-PEMFC[3–5]. In addition to the low level of performances achievable, the durability of HT-PEMFC is a major challenge, as most materials degradation processes are thermally activated. The main degradation mechanisms currently identified are the following ones: carbon corrosion[6,7], phosphoric acid leaching[6,8,9], membrane pinholes or creep and micro-fracture formation[10], degradation of carbon-supported Pt or PtM alloy (M being a 3d transition metal) nanoparticles (NPs) via agglomeration[6,9,11], metal alloy leaching[12], growth[9] and dissolution[10,13]. These degradations are largely reported in the literature (mainly for LT-PEMFCs, except for the phosphoric acid leaching), but there is still room to understand these degradations in HT-PEMFC devices and in particular the links that exist between performance degradations and nature of the catalysts and mode of solicitation of the cell.

To try to provide more insights into these aspects, the present study evaluates the degradations of Pt/C anode and PtNi/C cathode MEAs aged in al HT-PEMFC stack in start/stop operating conditions at 160°C. It specifically integrates startup and shutdown procedures designed for specific applications and details the physico-chemical characterizations of the catalyst layers before/after these procedures, which is not extensively studied for HT-PEMFC in the literature. One (representative) cell of the assembly was selected to perform *post mortem* characterizations and was fragmented in a way to distinguish the inlet and the outlet of gases – the reactants being fed in co-flow mode, in comparison to a new/pristine cell of the same batch. As the cells did operate in start/stop conditions, during the steps of start-up and shut-down, the inhomogeneity of distribution of the gases in the flow field may favor local fuel starvation phenomena and may accelerate the (local) degradations of the MEA, as widely investigated in LT-PEMFCs [14–16]. In this

study, performances degradations, catalyst carbon support and NPs material degradations are particularly under focus. Further, degradation mechanisms are proposed and linked to the damaging transition phases of the startup and shutdown procedures experienced by the cells.

EXPERIMENTAL SECTION

1. Membrane electrode assembly (MEA).

The MEAs studied here are commercial HT-PEMFC MEAs. They are composed on both sides of a gas diffusion layer (GDL) plus microporous layer (MPL) assembly, onto each of which is deposited a catalyst layer (CL); the separator and proton conductor is a phosphoric acid-doped polybenzimidazole (PBI) membrane. Sub gaskets are also present at the edge of the GDLs. The anode and cathode CLs are composite materials, made of Pt/C and PtNi/C, respectively, mixed with a polymer binder (presumably PTFE – the exact recipe of the MEAs is proprietary).

2. Operating conditions.

The MEAs analyzed in this study were tested in a short-stack operated at 160°C (aged MEA) or an equivalent new (pristine) MEA from the same batch. The cell design (notably the gas flow pattern and electrode area) is proprietary, but one notes that H_2 and air (O_2), introduced with stoichiometry values of 1.2 and 2.0, respectively, are essentially fed in co-flow configuration (the H_2 and air inlets face each other, idem for the outlets). The stack was aged with multiple steps of start-up and shutdown and constant current phases; the precise procedure is proprietary to Safran Power Units, but the gas configurations of the cell in transition phase are illustrated in Figure 1. The startup ON_C_Air consists of the introduction of air at the cathode side after the total introduction of H_2 in the anode compartment; ON_A_H_2 is the opposite, with the introduction of H_2 after the cathode have been totally flushed by air. For shutdown processes, oxygen on cathode

side is first eliminated, in OFF_N_2 by a N_2 flushing and in OFF_Air by the electrochemical reduction, the anode side being continuously supplied with H_2. In the last procedure (OFF_Air), after the consumption of the remaining oxygen, there was principally N_2 and H_2O in the cathode compartment.

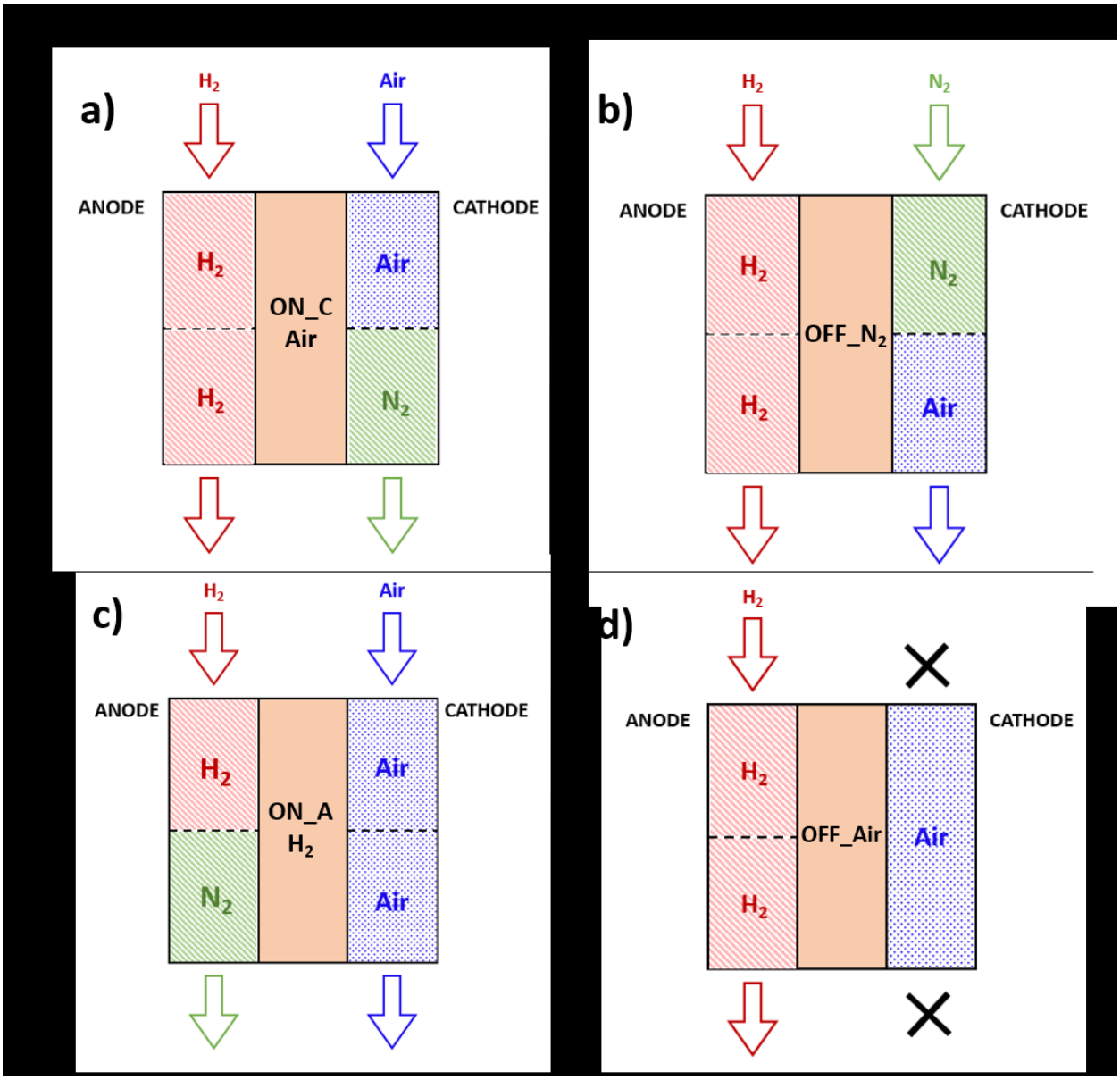

Figure 1. Schematic configuration of cells transient steps in the start/stop procedure. The configurations will be named (a) ON_C_Air, (b) OFF_N_2, (c) ON_A_H_2 and (d) OFF_Air in the following discussion.

The total duration of the test was around 900 h, with 800 cycles of the previously-described start/stop cycles and 28 h in constant current (14 h at 0.2 A/cm^2 and 14 h at 0.4 A/cm^2). The cycle of startup and shut down is illustrated in figure 2. For some cycles, a measure of CO_2 at the cathode inlet and outlet of the cell was performed. In the end, the whole aged MEA has experienced the successive start-stop and shut-down procedures, and has been analyzed *post mortem*, in comparison to similar analyses for an equivalent new MEA.

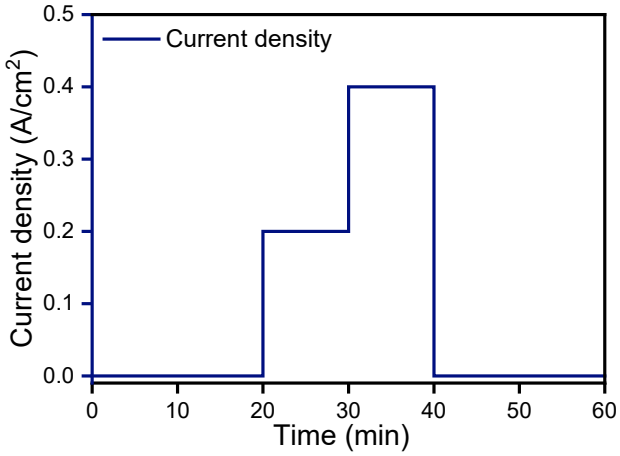

Figure 2. Schematic representation of one startup and shut down cycle.

3. *Pre* and *Post mortem* electrochemical characterizations.

The electrochemical characterizations of the CL materials were performed at *pre* and *post mortem* stage in a classic Rotating Disk Electrode (RDE) set-up with a Biologic SP-150 potensiostat. The RDE set-up is made of a thermostatic bath maintaining the electrochemical cell at 25°C (Julabo 200F), purged with Ar, O_2 or CO using appropriate gas manometers and pipes.

The 3-electrode cell is composed of gas inlet to the bottom of the cell to purge the entire electrolyte and a gas outlet linked to a bubbler to control the gas flux. A homemade hydrogen reference electrode (RHE) connected to a lugging capillary enables to polarize the working electrode (WE), the counter electrode (CE) being a Pt grid. The WE is a RDE equipped with a glassy carbon tip onto which the catalyst is deposited, in thin-film configuration. The "active layer" is prepared with scrapped catalyst from new/aged MEAs, formulated into an appropriate ink.

For the ink preparation (similar procedure for anode and cathode characterizations), the GDL and MPL were firstly removed thanks to liquid nitrogen, which enables to recover the CL and membrane without degradation. Then, the CL and membrane assembly was immersed in a beaker containing water maintained at 80°C to remove the majority of the phosphoric acid (PA) contained in these components: the PA removal was controlled by analyzing the pH of the solution, water being changed until stable pH. Then 5 mg of scrapped CL was mixed with 1.8 mL of ultrapure water Milli-Q, 523 µL of isopropanol (IPA) and 27 µL of Nafion™ 5wt% solution, and then ultrasonicated for at least 1 h in an ultrasonic bath. Finally, 10 µL of the ink was drop-casted on the glassy carbon tip of the RDE and the solvents evaporated, using the procedure described in [17]. It must be noted that it was initially tried to elaborate inks without any added Nafion™, but it was very difficult to disperse the catalyst material to form a homogeneous ink and no good deposit on the glassy carbon tip could be achieved, hence the present procedure.

Electrochemical measurements were carried out in 0.1 M perchloric acid (ultra-pure $HClO_4$) electrolyte; this acid was chosen to limit as much as possible poisoning by anionic species of the electrolyte and access to the intrinsic characteristics of the new/aged catalysts.

Cyclic Voltammetry (CV)

CV was performed in Ar-purged electrolyte. After a conditioning (*ca.* 80 cycles at 500 mV/s), 3 CV cycles were performed at 20 mV/s between 0.05 and 1.23 V_{vsRHE}. The electrochemical active surface area (ECSA) was determined by integration of the charge under the protons desorption area corrected from the carbon double layer (Hupd CV) [6]. The shape of this region also gives information about the catalyst nature (Pt or Pt-alloy).

CO-Stripping

CO-Stripping is a well-known characterization method to determine the ECSA and to qualitatively assess the morphology of a catalyst. CO gas was purged into the electrolyte for 5 min (CO adsorption) and then Ar was introduced for 30 min to remove the excess CO from the electrolyte under potential control (0.1 V_{vsRHE}). Then, 3 CV cycles were performed at 20 mV/s as for CV Hupd. It is generally considered as a better characterization for ECSA than CV of Hupd, especially for alloys[18,19], because of the strong adsorption of CO onto the catalyst sites and its sensitivity to the catalyst nature and morphology[20–22] (main peak potential, presence of a pre-peak), all these information being not available with Hupd CV.

Oxygen Reduction Reaction (ORR)

The performance of the cathode catalyst for the O_2 reduction reaction (ORR) was determined by appropriate CVs characterization. This reaction being the limiting one in a HT-PEMFC[23] , its degradation is the main factor of the loss of performances of the cells. It was performed by a slow-scan CV between 0.2 and 1.23 V_{vsRHE} at a scan rate of 5 mV/s in a O_2-saturated electrolyte at 1600 rpm. The diffusion-limiting current was corrected to extract the kinetic current, thanks to the Koutecky-Levich law (equation 1):

$$\frac{1}{j_{tot}} = \frac{1}{j_k} + \frac{1}{j_{diff}} \quad [1]$$

Where j_{tot} is the total measured faradaic current density, j_k is the kinetic contribution and j_{diff} is the diffusion-convection (mass-transport) contribution. The kinetic current was compared between each sample at 0.9 V_{vsRHE} to analyze performances degradations.

4. *Pre* and *Post mortem* physicochemical characterizations.

Scanning Electron Microscopy (SEM)

Cross-section of MEAs were prepared by cryo-fracture thanks to liquid nitrogen and observed using a FESEM instrument (Zeiss Ultra 55) equipped with Energy-dispersive X-ray spectroscopy (X-EDS – Bruker, with a silicon drift detector, Bruker – SDD). The obtained micrographs enabled to determine the adhesion of the CLs onto the PBI membrane and the thickness of these components. As the (proprietary) commercial MEA materials used present non-negligible inhomogeneity of catalyst layers thickness, thickness measurements were derived from statistical analyses of the micrographs, with average thickness values and error bars. The X-EDS quantitative mapping allows to show chemical (F, P, Ni and Pt) heterogeneities and compare their repartition *pre* and *post mortem*. The X-EDS maps were acquired at an acceleration voltage of 15 kV with a current of 3 nA. Maps were recorded for 30 min in average with drift correction. A quantitative analysis post-processing was performed on these maps with the model P/B Zaf proposed by Bruker in order to limit the interference between P (K shell at 2.010 keV) and Pt (M shell at 2.050 keV).

Transmission Electron Microscopy (TEM)

TEM catalyst observation is popular for PEMFC materials (carbon-supported catalyst NPs) and especially for comparison of the materials *pre* and *post mortem* morphologies [15,24–27]. Here, the NPs characteristics (size, density on the carbon support, extent of agglomeration) and carbon support morphology were investigated by TEM, using a JEOL 2010 apparatus operated at 200 kV; the chemical elements of the observed area were determined thanks to X-ray energy dispersive spectroscopy (X-EDS - INCA detector), used to identify the chemistry and potential metal leaching of the PtNi alloyed cathode catalyst [27]. In any case, the observed sample was prepared by depositing a drop of the scrapped catalyst ink used for electrochemical measurements onto a Cu grid with a Lacey-carbon membrane.

Inductive Coupled Plasma Mass Spectrometry (ICP-MS)

ICP-MS is commonly used to quantify metal composition and especially for PEMFC to quantify Pt and its alloy metal as Ni [14]. A protocol of mineralization of inks was applied to dissolve Pt and Ni: 30 µL of the ink prepared for electrochemical measurements were introduced in a clean PTFE tube and the solvent were evaporated in an oven for 5 min at 90°C. Then, 10 mL of aqua regia were added, the mineralization being performed in a microwave oven (CEM MARS), using a 30 min ramp to reach 200°C, a stabilization step of 5 min at 200°C, a 5 min ramp from 200°C to 220°C and a stabilization of 30 min at 220°C. Once the temperature has returned to the ambient, the mineralized solution was pipetted and 40 mL of water was added to rinse the mineralization PTFE tube. The solution obtained was then analyzed thanks to a PerkinElmer NexION 2000 ICP-MS set-up. The Pt weight resulting from this analysis gives access to the Pt loading deposited on

the glassy carbon tip electrode for electrochemical characterizations and then to the catalyst ECSA (expressed in m^2_{Pt}/g_{Pt}). The knowledge of the Pt and Ni weights allows to quantify of Pt/Ni ratio *pre* and *post mortem* for the cathode catalyst and to detect potential Ni leaching from the cathode catalyst.

X-ray Diffraction (XRD)

XRD is generally used to characterize the crystallographic structure of materials. Performing XRD on the cathode CL enables to identify possible change of alloying degree of the PtNi cathode catalyst caused by Ni leaching [27–29] *post mortem*. Assuming the variation of lattice parameter *versus* Ni content follows Vegard's law[27], the degree of dealloying was calculated via equation 2.

$$x_{(Ni)} = \frac{a_o - a_{exp}}{a_{alloy} - a_o} \quad [2]$$

in which a_o and a_{alloy} are the lattice parameter of Pt and PtNi (3.916 Å for Pt and 3.816 Å for PtNi), respectively and a_{exp} is the lattice parameter from catalyst analyzed. For the sample preparation, GDL and MPL were removed in liquid nitrogen and PA was in majority removed as described above. Then, the CL was scrapped and placed in a silicon support and analyzed thanks to a X'Pert Pro MPD diffractometer from Malvern, with a Cu (Kα) radiation source (1.5418 Å) in the conventional Bragg-Brentano geometry.

Raman Spectroscopy (RS)

Raman spectroscopy is a technique that analyzes the vibrational modes of molecules or crystal lattices with a monochromatic light source (LASER). In this study, RS was used to study the carbon support structure of the CL[30–32]. According to [33–35], RS allows to identify carbon structure variation by the analysis of at least 2 bands: D1 at 1350 cm^{-1} and G at 1585 cm^{-1} [14,36]. The sample used was a MEA cryo-fractured in liquid nitrogen without GDL and MPL, keeping PA to preserve the sample's structure for the analysis. Spectra have been obtained on the cross-section sample for cathode CL and anode CL. Measurements were performed with a Renishaw InVia spectrometer in micro-configuration (objective x50) operating at the wavelength of 785 nm (selected for optimal spectra resolution) and the power received by the sample was adjusted to 1.4 mW to prevent heat-induced degradations.

X-ray photoelectron spectroscopy (XPS)

X-ray photoelectron spectroscopy, enabling to analyze the surface chemistry of materials, was carried out on cross-section of electrodes thanks to a K-Alpha apparatus from Thermo-Fisher Scientific. The sample surfaces were irradiated with Al Kα radiation (1486.6eV) in a UHV chamber (10^{-9} mbar), the ejected electrons being collected by a hemispherical analyser at 30 eV constant pass energy. The energy scale was calibrated with the C 1s line from the contamination carbon at 285.0 eV. Analyses were carried out at constant angle, 90°, between the sample surface and the analyser. Pt, F, P, O and C were precisely analyzed in their respective energy window.

RESULTS

1. Performance degradation.

Along the test life of the stack, various couple of startup (labelled D) and shutdown (labelled A) procedure, represented in Figure 1, were performed one after the other, interspersed with N_2 storage periods, as explained in M. Durand thesis[37] from which the aging data originate. Sessions of 50 or 150 startup and shut down cycle were successively carried out without interruption on the same short stack. Polarization curves were performed before and after each session to quantify the performance loss due to the repeated A/D sequences. It should be noticed that a technical issue on the test bench rendered impossible the N_2 flushing in the procedure ON_A_H_2/OFF_Air for approximatively 20 cycles during the last session of the ageing test.

Hereafter, a comparison of the degradation rate corresponding to each D/A couple is analyzed; the relative percentage of cell voltage loss per start/stop cycle is given in Figure 3.

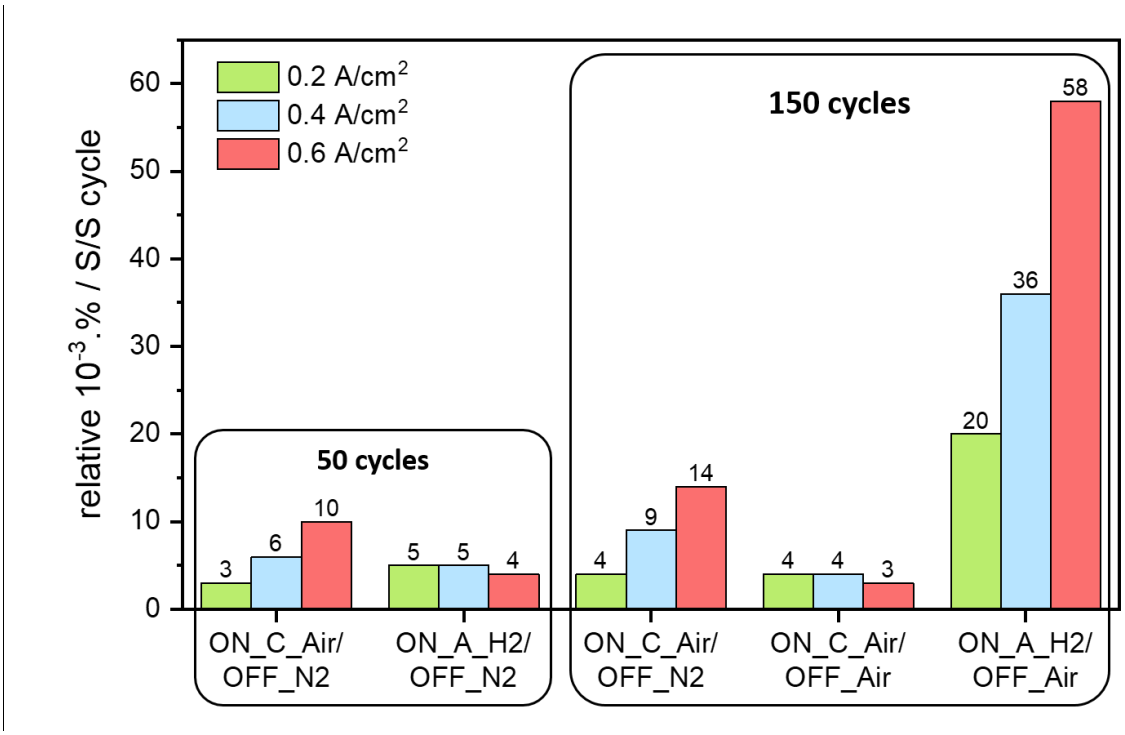

Figure 3. Relative percentage of cell voltage loss after a set of 50 or 150 cycles for each procedure combination. The percentage are indicated for 3 operating point: j = 0.2 (green), 0.4 (blue) and 0.6 (red) A/cm^2.

ON_C_Air/OFF_N_2 vs ON_A_H_2/OFF_N_2 (for 50 cycles): at low current density (0.2 A/cm^2) the startup ON_A_H_2 seems a little more degrading than ON_C_Air, while at higher current density (0.6 A/cm^2), ON_C_Air/ OFF_N_2 led to higher performances loss than ON_A_H_2/ OFF_N_2. No obvious differences are noted at intermediate current density (0.4 A/cm^2).

ON_C_Air/OFF_Air vs ON_A_H_2/OFF_Air (for 150 cycles): the degradation rate is clearly larger for the couple ON_A_H_2/OFF_Air than ON_C_Air/OFF_Air. However, this statement should be mitigated, owing to the problems in the N_2 flushing during the ON_A_H_2/OFF_Air procedure mentioned above. One notices that the ON_C_Air startup procedure coupled with OFF_Air leads to minimal loss of performance, regardless of the investigated current density, which is at variance compared to the previous comparison with

OFF_N_2 shutdown couples. In addition, the couple ON_A_H_2/OFF_Air seems to imply very different level of performances degradation in function of the current density, which was also not the case with the shutdown OFF_N_2.

ON_C_Air/ OFF_N_2 vs ON_C_Air/OFF_Air (for 150 cycles): ON_C_Air/ OFF_N_2 and ON_C_Air/OFF_Air leads to the same degradation rate at low current density (0.2 A/cm^2). However, the couple ON_C_Air/OFF_N_2 seems to induce more severe degradations at intermediate current density and even more at high current density than ON_C_Air/OFF_Air. It agrees with the previous observations for ON_C_Air/ OFF_N_2 couple (for 50 cycles).

To summarize, the main observations given by the comparison of startup and shutdown couples are as follows: ON_A_H_2 is more degrading at low current density than ON_C_Air; the couple ON_C_Air/ OFF_N_2 induces higher degradations at higher current densities and it could not be attributed to ON_C_Air or OFF_N_2 only; the ON_A_H_2/OFF_Air couple is the more severe procedure regarding performance degradations and especially at high current density.

CO_2 emissions measurements were also performed during these tests: significant peaks in CO_2 concentration were detected only for the ON_A_H_2 and OFF_Air procedures, indicating that these are the most degrading for the carbon support of the catalysts. On the contrary, procedures ON_C_Air and OFF_N_2 do preserve the carbon support (they do not generate major carbon corrosion), so the larger performances loss at high current density observed in the couple ON_C_Air/ OFF_N_2 previously should not be caused by a major carbon corrosion and subsequent collapse of the porous structure of the active layer (that would have a non-negligible impact on the mass-transport of gases), as that noted by Durst et al.[38]. During ON_A_H_2 and OFF_Air, the non-negligible CO_2 emissions are attributed to the carbon support corrosion of the cathode CL and

should be responsible in part to the higher rate of performances degradation observed operating with the combination of procedures ON_A_H_2/OFF_Air. The large carbon corrosion should stimulate secondary catalyst degradations phenomena, such as agglomeration of NPs and their disconnection from the carbon support[39,40]. This was further analyzed thanks to *pre* and *post mortem* characterizations (TEM, SEM).

2. Carbon support corrosion.

Post mortem characterization of the carbon support functionalization and corrosion were performed, specifically at the interface with the metal NPs. The first steps of the carbon corrosion correspond to formation of carbon-oxygen surface groups[35] (surface functionalization), which can ultimately lead to carbon oxidation into CO_2; it is thermodynamically possible above 0.207 V_{vsRHE} and only kinetically proceeds above 0.6 V_{vsRHE} at the interface with Pt NPs (above 1.0 V_{vsRHE} in absence of catalyst nanoparticles)[15]. Carbon corrosion is likely to induce a modification of the carbon support morphology and porosity. At a larger scale, the modification of the porosity could have an impact on the thickness of the electrode, because of local collapses in the porous structure [38,40,41]. The thicknesses of each layer of the MEA were measured on SEM cross-section images as an average of at least 4 areas in the layer (Figure 4). The significant irregularity of the electrodes, damaged mainly by carbon fibers of GDL, led to large errors bars for these thickness measurements and conclusions have to be moderate. This being admitted, one could conclude that, whether for the anode or the membrane, no significant variation could be noticed before and after the ageing test. For the anode, no significant thickness variation was expected, because the potential reached by this electrode in operation is not critical for carbon corrosion. However, regarding the cathode, even if error bars stay very large, there is a significant decrease of the CL

thickness, and this is especially evident at the cell outlet. This variation could be a sign of a significant carbon corrosion and should be related to the emissions of CO_2 detected in the startup ON_A_H_2 and shutdown OFF_Air phases.

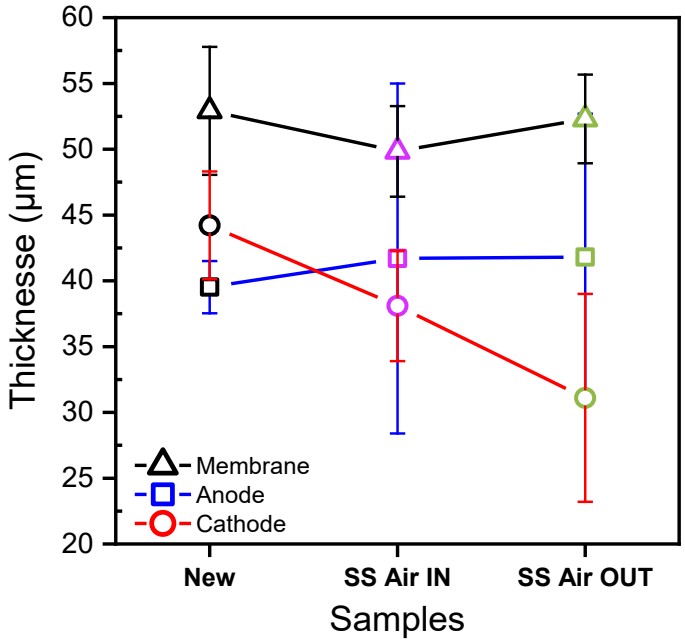

Figure 4. MEA anode (square), cathode (circle) and membrane (triangle) mean thicknesses calculated from at least 4 areas measured on SEM cross-section images for the pristine (New) state and after the aging procedure (in that case in the air inlet and outlet regions).

Semi-quantitative SEM X-EDS mapping of Pt is an indirect way to highlight potential carbon corrosion. In Figure 5, the Pt concentration in aged MEAs versus the new one seems in average slightly higher at the anode, but largely higher for the cathode. One could posit that the non-negligible roughness of the cryo-fractured sample could disturb the signal received by the X-EDS detector (for example red points at the anode in Figure 5b). However, having taking into account these artifacts, there is still much higher concentration of Pt in aged samples for the cathode CL. Because obviously no Pt was created during the test, this means that the concentration

of other elements did decrease: either the carbon support or the polymer binder (or both) must have "disappeared" to some extent. X-EDS cannot reliably quantify light element as C and F, so no quantified mapping was performed on these elements. However, the previous conclusion derived from the change of electrode thickness enables to state that the large difference of Pt concentration found in the cathode mapping should come from a large elimination of carbon support by carbon corrosion (and this agrees with the CO_2 detection during some of the periods of the aging test). Furthermore, no obvious difference between inlet and outlet could be noticed here whether it is for the cathode or the anode (red areas are measure artefacts).

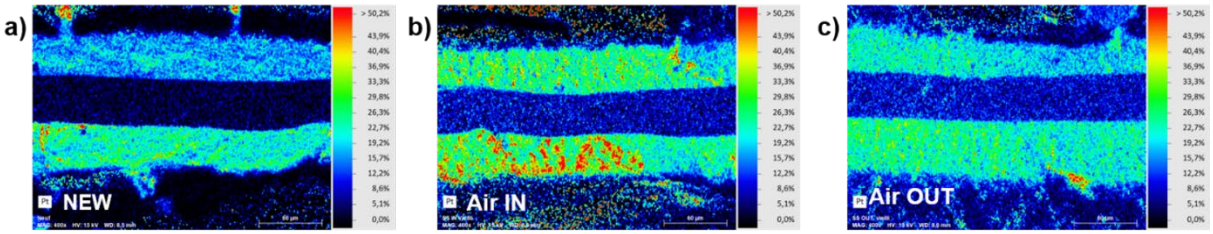

Figure 5. Pt cross-section quantified mapping of (a) fresh, (b) aged air inlet and (c) aged air outlet MEA. The wt% scale was kept at the same level (from 0wt% in dark/blue to 50 Pt wt% in red area) for each sample. Anode and cathode are respectively at the bottom and at the top of cross-section images. The value of Pt concentration should not have to be taken in absolute value of the Pt concentration in CL, only by a way of comparison.

Before irreversible oxidation of carbon into CO_2, carbon degradation starts with creation of defects in its structure (functionalization), which facilitates the migration of Pt nanoparticles and their agglomeration[39]. To identify carbon structure variation, Raman spectroscopy was performed on cross-sectioned MEAs prepared by cryo-fracture (Figure 6).

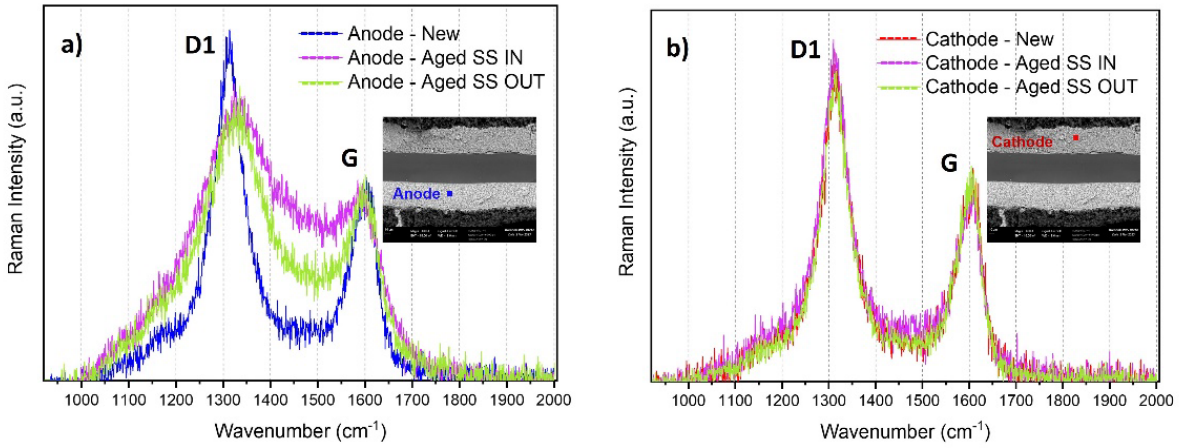

Figure 6. Raman spectra of (a) anode and (b) cathode new and aged gases inlet and outlet CL from cryo-fractured samples. The spectra have been treated by subtracting a linear baseline in the 900-2000 cm^{-1} range and then adjusted so that the G band amplitude remained constant.

The amount of defects in graphene can be derived from D1 band shape and intensity. More precisely, the intensity of D1 band (1350 cm^{-1}) corresponds to the crystallites size in graphene plane, while variation of its width is linked to the creation of point defects in the structure[30]. The G band (1595 cm^{-1}) corresponds to the crystalline structure without defects. Both bands are present for any type of carbon investigated here (new/aged, at inlet or outlet regions). Thanks to the normalization on the G band, the Raman spectra enable to identify a modification of the carbon structure, highlighted by the change of the D1 band. At initial state, the anode and cathode carbon structures are closer to a graphitized one than a largely amorphous one, because of the well-defined bands[30]. While no structure variation is detected by Raman spectroscopy for the aged cathode catalyst (Figure 6b), the aged anode catalyst has a significantly different signature (Figure 6a), which must be explained. The absence of modification of the Raman signature of the cathode carbon could be surprising at first sight, following the previous observations (CO_2 emissions and cathode CL thickness decrease); however, as the carbon that suffered corrosion was eliminated

(into CO_2), it is likely that the remaining carbon kept the initial structure (in other words, the topmost layer was corroded into CO_2, then exposing the next (pristine) layer). On the opposite, the larger variation of the anode carbon support structure is not frequently observed in the literature (usually made for tests involving continuous operation). One exception is the work of Touhami et al.[42], in which anode aging was observed, related to wet/dry cycles[38]. To better understand this variation, XPS experiments were carried out on CL in cross-section samples (Figure 7).

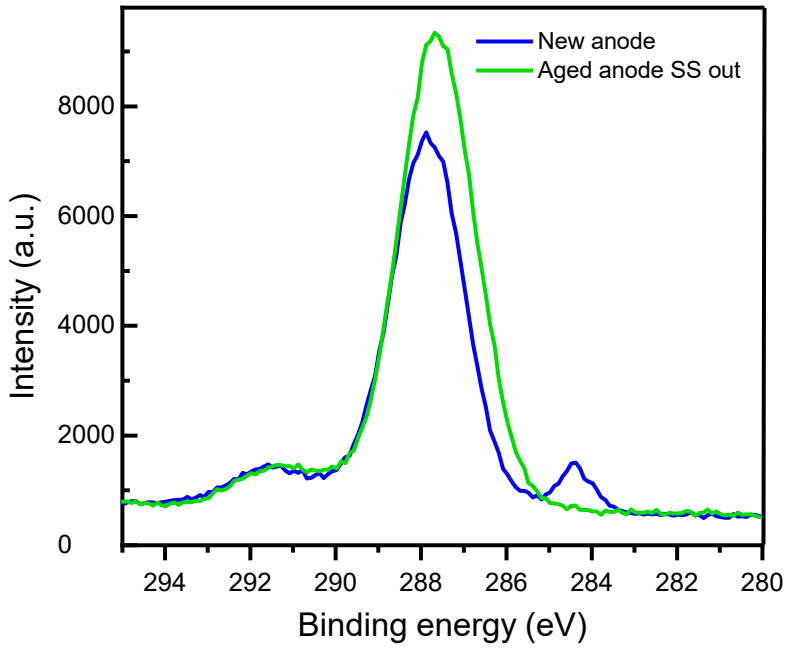

Figure 7. C1s spectra of XPS, for the anode CL carbon support, made on cross-section samples for a new and aged MEA (at the outlet region).

The main differences in carbon C1s XP spectra are the disappearance of the component at the binding energy 284.4 eV in the aged outlet anode sample and the relative different intensity of the peak at 287.8 eV. According to the literature[43], the component at 284.4 eV is the contribution of the C-C or C-H chemical binding and especially graphitized carbon according to Puziy et al.[44].

The presence of this component at the initial state agrees with Raman observations, with an initial more graphitized structure. Then, the loss of this contribution in the aged sample indicates a modification of the chemical binding and surface structure of carbon. It agrees with the structure modification monitored for aged samples in Raman spectroscopy. The component at 287.8 eV has a higher intensity for the aged sample and is slightly moved to lower binding energy. According to [43,44], this component is linked to C-O and C=O chemicals bonding. One hypothesis to explain these modifications of the carbon structure and binding is a large functionalization of the carbon support in operation at low potential, likely by interaction with chemical species such as phosphoric acid (this will be discussed hereafter). According to Parry et al., the component at 291.6 eV is the contribution of C-F_2 chemical bonding; this contribution comes from the presence of the polymer binder in contact with the carbon support and does not seem to change significantly in operation[31].

3. Catalyst nanoparticles (NPs) degradation.

According to Castanheira et al.[36], carbon corrosion and functionalization at the interface with Pt NPs accelerates the degradation of the catalyst NPs, leading to their agglomeration and stabilization between carbon grains, decreasing their density over the carbon surface and/or possibly inducing their detachment. These degradations were investigated thanks to TEM imaging and statistic measurement of the isolated NPs sizes. Figure 8 presents the (a) anode and (b) cathode isolated NPs size distribution measured on several representative TEM images; representative (c) TEM images of NPs supported on carbon, and (d) some huge agglomerates observed in some areas of the anode CL, *post mortem*, are also provided. Table 1 summarizes the mean diameter/size of NPs, calculated thanks equation 3 [45]:

$$\overline{d_n} = \frac{\sum_{i=1}^{n} n_i d_i}{n} \quad [3]$$

where $\overline{d_n}$ is the mean isolated NPs size (diameter), n_i is the number of NPs of diameter d_i, and n is the total number of NPs measured (> 100 NPs counted for each sample).

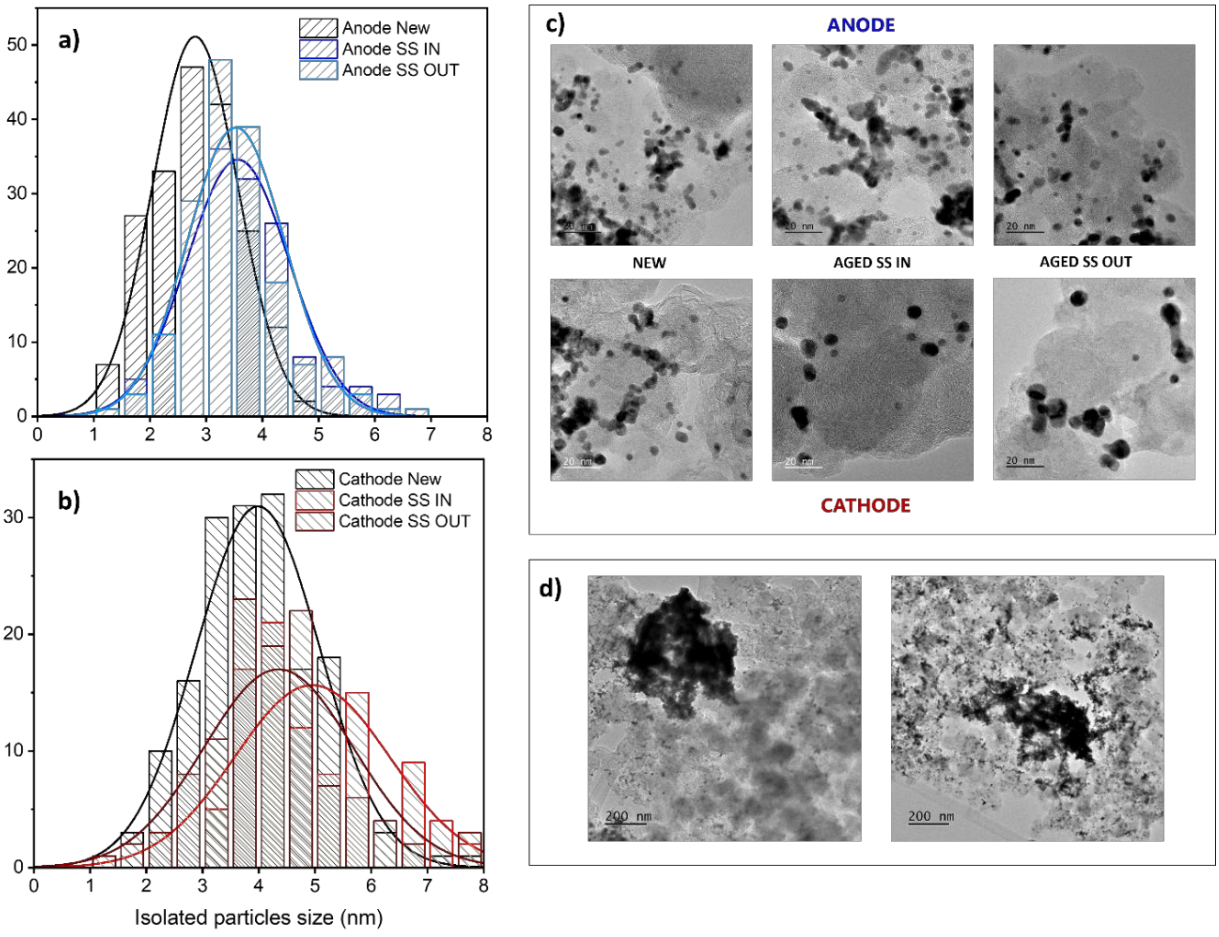

Figure 8. Anode and cathode CL morphological changes from TEM images, (a) and (b) are respectively the isolated NPs size distribution for the anode and cathode; (c) images of catalyst of new, aged gas inlet and outlet for both anode and cathode and (d) images of huge NPs agglomerates observed *post mortem* in the anode CL.

Table 1. Mean isolated NPs size measured on TEM images thanks to ImageJ software for new, aged in start/stop mode gases inlet (Aged SS IN) and gases outlet (Aged SS OUT).

Sample	Mean isolated particle size (nm)	
	Anode	*Cathode*
New	2.8 ± 0.6	3.9 ± 0.8
Aged SS IN	3.6 ± 0.7	4.9 ± 1.1
Aged SS OUT	3.5 ± 0.6	4.4 ± 0.9

At the initial state, the anode NPs are smaller than the cathode ones and less dispersed in size. After operation, both anode and cathode mean isolated NPs size increased (Figure 8a, 8b and table 1). The cathode NPs average increased significantly, especially at the gas inlet region, which, cumulated to the presence of small NPs even after operation, signs major Pt dissolution and Pt^{z+} redeposition, well known as Ostwald ripening and already reported as one the main process of degradation in the cathode potential range[26]. For the anode, the increase of isolated NPs size, the appearance of NPs agglomerates and the relative absence of very small NPs suggests particles aggregation (and possibly coalescence) as the main degradation mechanism.

The loss of isolated NPs density, according to TEM images is noticeable for both the anode and cathode catalysts. For the cathode, while there was a difference between the gases' inlet and outlet for isolated NPs size, there is no difference for the NPs density over the carbon support. Ostwald ripening stays consistent to explain the loss of isolated NPs density for the cathode, with few large agglomerates and instead greater amount of small (typically 2-5 particles) agglomerates.

These can likely originate from the carbon corrosion mentioned above, after which some Pt NPs detach, migrate on the carbon substrate and are collected/stabilized on nearby NPs. At the opposite, for the anode, the presence of light and huge (around 300 nm of diameter) agglomerates in Figure 8c and 8d, preferentially corresponds to a mechanism of intense NPs migration over the carbon surface (which is very functionalized) and coalescence in the reducing conditions experienced. The presence of such huge agglomerates was not often reported in the literature for anode CLs; in any case, these should likely non-negligibly decrease the anode active surface area.

The presence of agglomerates was also identified by CO-Stripping voltammetry (Figure 9). The peak close to 0.7 V_{vsRHE} (pre-peak) corresponds to less favorable adsorption sites, as grain boundaries present in aggregated particles, while the peak at higher potential (main peak) corresponds to isolated particles, which bind CO more strongly[20,21]. The non-negligible degree of agglomeration of the anode and cathode catalysts at the initial state observed in TEM images (Figure 8c) is confirmed by the presence of a pre-peak for the fresh catalyst at both the anode and cathode. This observation is rather unusual for initial catalysts (which normally bare more isolated nanoparticles[40,46]); it lets one think that some degradation of the catalysts occurred on the MEAs already during storage (after preparation and prior utilization); this corresponds to open circuit under oxygen, owing to the presence of phosphoric acid and ambient air, hence very oxidizing conditions compatible with the rather agglomerated "new" catalyst materials. For the aged anode catalyst, the double peak shape does not show significant variation compared to the initial state (Figure 9a and 9c), suggesting that most of the nanoparticles' agglomeration appeared before operation. For the cathode catalyst, there is a non-negligible variation of proportion area between pre-peak and principal peak in Figure 9b. Figure 9d, presenting raw data in current, allows identifying that this variation of proportion may mainly be ascribed to a large decrease of the

principal peak associated to isolated NPs. This observation agrees with the TEM observations: less isolated nanoparticles for the aged cathode catalyst and presence of small agglomerates. It confirms that Ostwald ripening (isolated NPs preferentially dissolved and redeposition of Pt^{z+} on larger ones) and local NPs migration into agglomerates of NPs are dominant for the cathode.

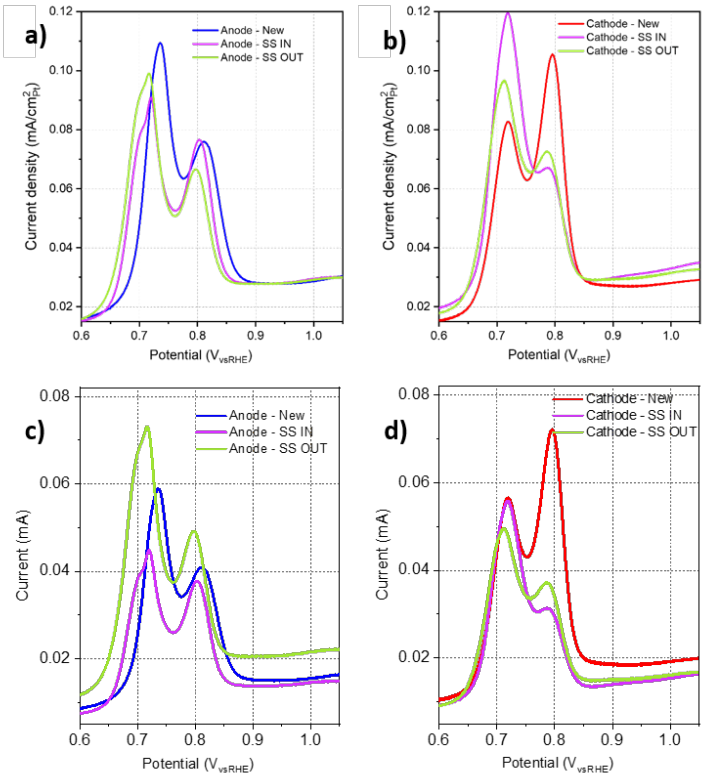

Figure 9. CO-Stripping features in current density for the (a) anode and (b) cathode and in current for (c) anode and (d) cathode. New and aged catalysts air inlet and outlet are represented using the RDE cell at 25°C in 0.1 M $HClO_4$ electrolyte at 20 mV/s.

Small or large agglomerates affect the isolated NPs density and decrease the catalyst surface area available for electrochemical reactions: the electrochemical active surface area (ECSA). Thanks to Hupd and CO-Stripping CVs, the ECSA was calculated for the catalysts *pre* and *post mortem* (Figure 10). In the gases' inlet region, while the ECSA decrease of the aged anode

catalyst is not significant and stays in the error bars versus the initial ECSA, the cathode ECSA significantly decreased during operation, by a factor *ca*. 4. This large decrease is likely the consequence of major dissolution of Pt nanoparticles into Pt^{z+} ions, followed by leaching of these Pt^{z+} ions downstream the cathode gas (additional Ni leaching is also possible), associated to minor nanoparticles growth following Ostwald ripening in this region. The carbon corrosion of cathode carbon support identified in the previous section should also participate to the decrease of the ECSA by Pt NPs detachment (and minor agglomeration into the small agglomerates detected in TEM and CO-stripping). All these processes are favored by the high cathode potentials reached in operation (especially at the cathode inlet), as already reported in the literature of LT-PEMFCs [14]. At the gases' outlet, no significant ECSA variation is observed for the cathode, while for the anode, the ECSA increased by a factor *ca*. 2 after operation. The large difference observed between the cathode gas inlet and outlet regions, could be explained by a variation of local potentials seen by the electrode during the alternating steps of startup and shutdown. As explained in the literature of LT-PEMFCs [15], alternating startup and shutdown steps may transiently create active and passive regions in the plane of the MEA, and local reversed currents (these *scenarii* will be further exposed in the discussion section).

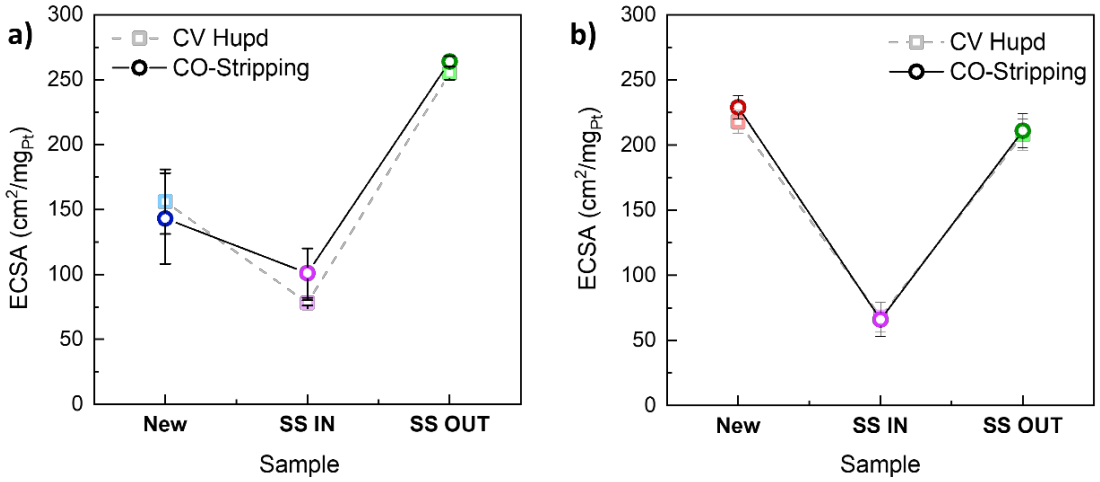

Figure 10. Electrochemical Surface Area (ECSA) of (a) anode and (b) cathode catalyst measured thanks to Hupd and CO-Stripping CVs for fresh and aged gases inlet and outlet catalysts in 0.1 M $HClO_4$ electrolyte at 25°C.

4. Ni leaching from PtNi alloy cathode catalyst nanoparticles.

The global catalyst degradations presented in the previous sections did show a difference in behavior between the anode (Pt/C) and cathode (PtNi/C) catalyst; Ni leaching from the cathode catalyst is possible, as shown in the literature both for LT and HT-PEMFCs [3]. The leaching is even larger in HT-PEMFC, because of the high operation temperature and phosphoric acid environment. Herein, the Pt/Ni ratio was tracked *pre* and *post mortem* by combining XRD, TEM X-EDS, ICP-MS, Hupd CV and ORR CV in RDE.

X-Ray diffractograms of the cathode catalyst (Figure 11b), show a clear variation of the alloy crystallite nature with a non-negligible dealloying of PtNi into an alloy richer in Pt: the lattice parameter is significantly larger for the aged catalyst and closer to pure Pt. In order to get quantitative data about the Ni leaching rate upon HT-PEMFC operation, the Pt/Ni atomic ratio was calculated thanks to the following quantitative characterizations techniques: TEM X-EDS, ICP-

MS and XRD Vegard's law (Figure 11a). While at the initial state, all techniques point to the same level of alloying ratio (close to Pt_3Ni alloy), for the aged catalyst, each technique suggests non-negligible deviation in the dealloying rate. Considering errors bars, there is especially a deviation between the group X-EDS and ICP-MS versus XRD, the former pointing to the larger presence of Pt compared to Ni (*ca*. 7:1 and 5:1 at the inlet and outlet regions, respectively). Such difference was already reported in the literature[27,28], and was attributed to the nature of the material analyzed: XRD scans only the crystalline lattice of the catalyst and not the whole material composition. Hence, the smaller remaining Ni content measured by X-EDS and ICP-MS versus XRD overall suggests that some Ni (and maybe Pt) might not be present in the crystalline lattice *post mortem*, likely dissolved as ions (Ni^{2+}, Pt^{z+}) in PA, this dissolution originating from the surface (and not from the crystalized bulk) of the NPs. As Ni^{2+} is not capable to be reduced to Ni metal in the environment of a PEMFC[47], it is no surprise that Pt "concentrates" *post mortem* versus Ni overall, even though the crystalline core of the PtNi NPs seem richer in Ni than the overall CL (where Ni^{2+} ions are likely diluted in the PA). This observation is especially true at the gas inlet.

The variation of morphology of the proton desorption area of the cathode catalyst Hupd CV supports previous observations on Ni leaching (Figure 11c). Aged catalysts (whether at gases inlet or outlet) show proton desorption peaks closer to the features of pure Pt catalyst (sharper Hupd peaks) compared to the initial state, in which the Hupd features are less defined, a behavior also observed in [48] for PtCo/C catalysts operated in LT-PEMFCs.

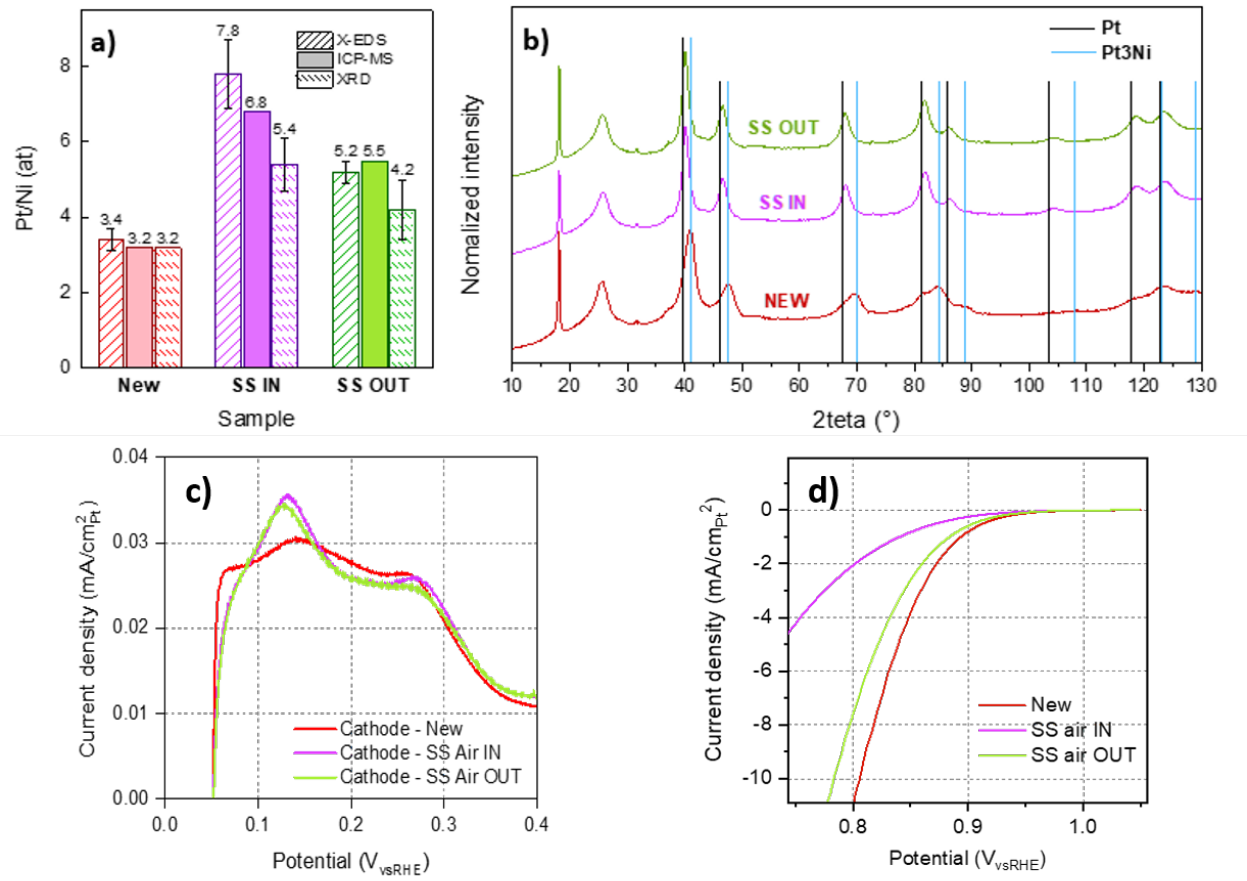

Figure 11. (a) Pt/Ni atomic ratio calculated from X-EDS analysis with TEM, ICP-MS analysis and XRD thanks to Vegard's law from cathode new and aged gases inlet and outlet catalyst ; (b) diffractogram of cathode catalyst with the diffraction peak position of Pt and alloy PtNi ; (c) Cathode catalyst Hupd region from CV measurement at a scan rate of 20 mV/s, at 25°C, in 0.1 M $HClO_4$ electrolyte ; (d) Cathode catalysts kinetic current density for ORR measured with a scan rate of 5 mV/s at 25°C, in 0.1 M $HClO_4$ electrolyte.

The leaching of Ni from the cathode catalyst, in addition to the loss of ECSA at the gas inlet (Figure 10b), are in part responsible for the global cell performance degradation. More precisely, it explains the ORR performances decrease (Figure 11d). While for fresh catalyst at 0.95 V_{vsRHE}, the ORR kinetic current density reaches 0.090 ± 0.005 mA/cm$^2_{Pt}$, it is only 0.050 ± 0.010

mA/cm^2_{Pt} and 0.075 ± 0.005 mA/cm^2_{Pt} for the aged catalyst at the air inlet and air outlet, respectively. The aged gas inlet catalyst is significantly less efficient than the gas outlet one, owing to (i) the more important Ni leaching rate presented in Figure 11a in the cathode inlet region and (ii) the presence of larger Pt nanoparticles (following Pt^{Z+} redeposition and/or Ostwald ripening) at the outlet – larger Pt nanoparticles being more active for the ORR than smaller ones[49–52] .

The more severe catalyst degradations at the cathode inlet (larger Ni leaching and ECSA loss), is explained by the more oxidizing environment of the cathode inlet region, which originates from the higher concentration of O_2 (and lower concentration of water) at the gas inlet as reported in the work of Dubau et al.[14] for LT-PEMFC.[12] It should be also more acidic, because of the dilution of phosphoric acid at the cell outlet: the water produced in operation is driven by the gas flux to the outlet, PA loss being largely reported in literature[6,8,9].

DISCUSSION

Multiple stresses and various operating conditions were applied to the cell during the aging test, and then various type of catalyst degradations were monitored. Hereafter, the degradations observed will tentatively be linked to the operating conditions experienced.

One of the main obvious degradations observed is the modification of the cathode catalyst, especially at the inlet of the cell: ECSA decrease (Figure 10b), dissolution of isolated NPs (CO-Striping, Figure 9d) or catalyst de-alloying by a Ni leaching (Figure 11) all imply a large reduction of the ORR performances of the inlet catalyst in RDE configuration (Figure 11d). These degradations typically come from the dissolution of Pt and Ni of the mother alloyed PtNi NPs into Pt^{z+} and Ni^{2+} cations. Pt^{z+} can redeposit on larger/more stable NPs (Ostwald ripening mechanism) and participate to the growth of NPs (Table 1) and the increase of their extent of aggregation. This

mechanism is more pronounced at the inlet of the cell, owing to the more oxidizing and acidic media, locally. One associates this mechanism principally to operating phase at constant current between the steps of startup and shutdown (the time spent at constant current for each step is approximatively 20 min). One hypothesis is that the cathode inlet is more prone to Pt and Ni dissolution in operation and the produced metallic cations at the inlet could be redeposited at the outlet of the cell and provoke a local "recovery" of ECSA (whether for anode and cathode). The mechanism is illustrated in Figure 13: the major generation of Pt^{z+} ions in the cathode inlet region induces, by gas flow, concentration gradient or migration, Pt^{z+} transport downstream (to the cathode outlet region). At the outlet – owing to the less oxidizing conditions in the O_2-depleted gas and more water-rich phosphoric acid – these species can be redeposited on the larger Pt particle/agglomerates. This means that Pt^{z+} transport also proceeds from the Pt^{z+}-rich cathode across the PBI membrane, via diffusion in open-circuit or migration under load; these species are then easily reduced on the existing Pt/C anode catalyst, owing to appropriate (reducing) thermodynamic potential conditions[14,46]. The mechanism could explain the relative stability of the ECSA at the cathode outlet and the increase of ECSA at the anode outlet.

The catalyst dissolution should also be accelerated by the startup and the shutdown phases experienced by the cell, during which it is maintained in open-circuit (no external current generation). In these transients, a H_2/N_2 front exists at the negative electrode (normally the anode) or O_2 (air)/N_2 front at the positive electrode (normally the cathode), that leads to partition of the cell in an active region (operating like a fuel cell, the one regularly fed by H_2 and O_2 (air) at the negative/positive electrodes, respectively) and a passive (operating like an electrolyser) region (the one with N_2 either at the positive or negative electrode). The electrodes being isopotential (owing to the high electronic conductivity of the bipolar plates and GDLs) and the electrolyte being not

(owing to its much smaller ionic conductivity), the active region imposes a potential difference between the 2 electrodes that can result to local reversed current in the passive region, as described for LT-PEMFC in the past [53,54].

Such internal currents are likely to exist in the ON_C_Air and OFF_N_2 sequence, although in first approximation, it seems rather not critical. Indeed, even if protective flush of N_2 was introduced at the cathode inlet in the transition phase (OFF_N_2), the voltage of the entire cell stays close to 1 V owing to the presence of H_2 at the negative electrode and O_2 at the positive one. In the passive region, the negative electrode (anode) compartment maintains at a potential close to 0-0.3 V_{vsRHE} in presence of H_2 and phosphoric acid (the latter can reduce into H_3PO_3 quite easily [55]), hence, the positive electrode (cathode) must stay at 1-1.3 V_{vsRHE}, which can induce minor oxidation or dissolution of Pt and/or of carbon (Figure 12a). Prokop et al [56] reported that the dissolution of Pt is accelerated in H_3PO_4 HT-PEMFC by the harsh acidic medium and high temperature, Pt dissolution being emphasized in the vicinity of the H_3PO_4 molecules. Although ON_C_Air startup is by itself not degrading, succession of ON_C_Air and OFF_N_2 induces repeated sequences of Pt-oxidation/reduction at the positive electrode, where the mechanism of Pt-O place exchange promotes temperature-enhanced dissolution of Pt into Pt^{2+} and Ni into Ni^{2+} [57]. The observed performances degradation during the ON_C_Air/OFF_N_2 procedure, that corresponds to significant decrease at high current densities, is compatible with a severe reduction of mass-transport properties of either H^+ or O_2, that is likely promoted by the metal cation production during the transients; in that process, the interaction of the produced cations with H_3PO_4 molecules, which can form complex molecules, likely limits the O_2/H^+ transport to the catalyst NPs surface and reduce mass-transport rate; this deleterious effect of dissolved metal cations had also been observed in LT-PEMFC [58].

a)

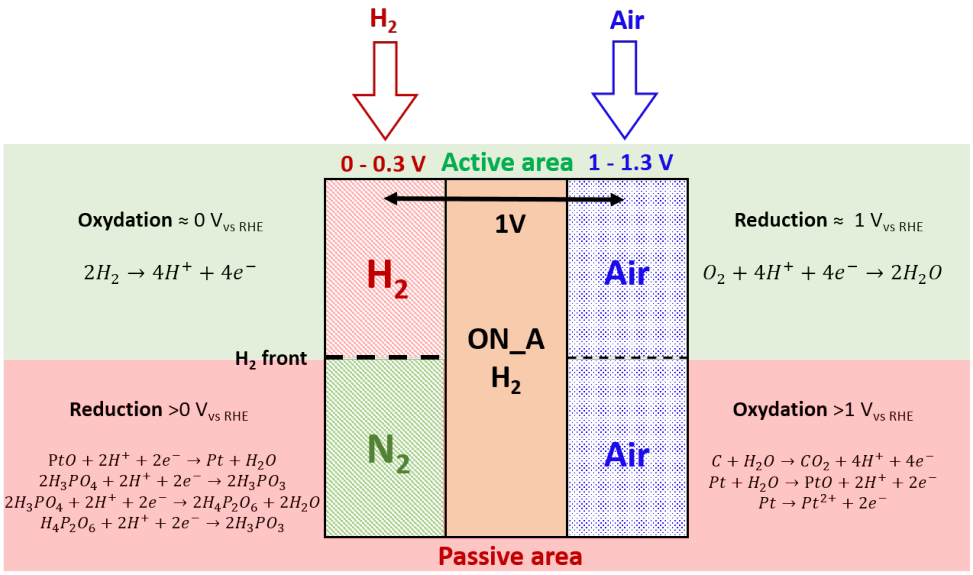
H2
Air
0 - 0.3 V
Active area
1 - 1.3 V
Oxydation ≈ 0 Vvs RHE
2H2 → 4H+ + 4e−
1V
H2
Air
ON_A
H2
Reduction ≈ 1 Vvs RHE
O2 + 4H+ + 4e− → 2H2O
H2 front
Reduction >0 Vvs RHE
PtO + 2H+ + 2e− → Pt + H2O
2H3PO4 + 2H+ + 2e− → 2H3PO3
2H3PO4 + 2H+ + 2e− → 2H4P2O6 + 2H2O
H4P2O6 + 2H+ + 2e− → 2H3PO3
N2
Air
Oxydation >1 Vvs RHE
C + H2O → CO2 + 4H+ + 4e−
Pt + H2O → PtO + 2H+ + 2e−
Pt → Pt2+ + 2e−
Passive area

b)

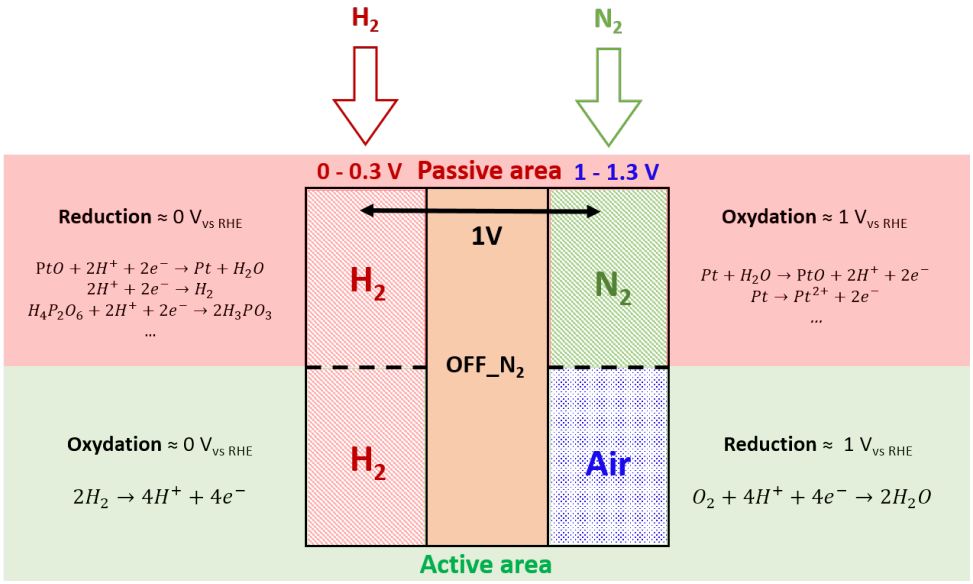
H2
N2
0 - 0.3 V
Passive area
1 - 1.3 V
Reduction ≈ 0 Vvs RHE
PtO + 2H+ + 2e− → Pt + H2O
2H+ + 2e− → H2
H4P2O6 + 2H+ + 2e− → 2H3PO3
...
1V
H2
N2
OFF_N2
Oxydation ≈ 1 Vvs RHE
Pt + H2O → PtO + 2H+ + 2e−
Pt → Pt2+ + 2e−
...
Oxydation ≈ 0 Vvs RHE
2H2 → 4H+ + 4e−
H2
Air
Reduction ≈ 1 Vvs RHE
O2 + 4H+ + 4e− → 2H2O
Active area

c)

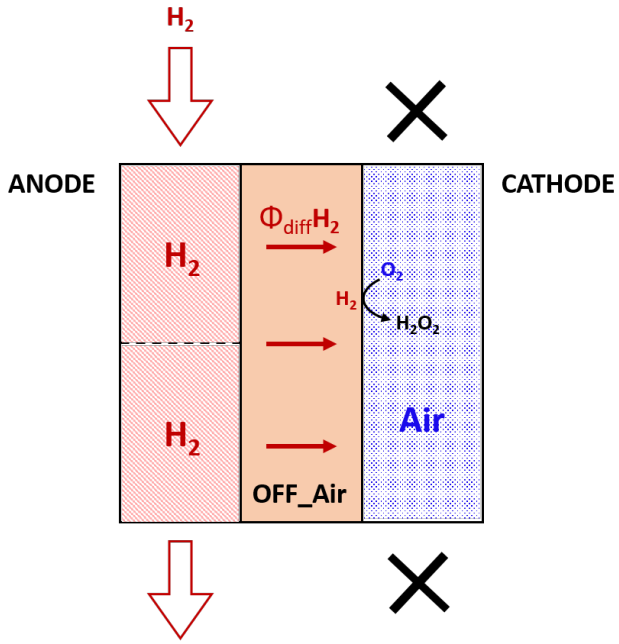
H2
ANODE
CATHODE
ΦdiffH2
H2
O2
H2
H2O2
H2
Air
OFF_Air

Figure 12. (a) Illustrative scheme of degradation reactions, which could occur in the startup procedure ON_A_H_2. **(b)** Illustrative scheme of degradation reactions, which could occur in the shutdown procedure OFF_N_2. The reverse current in the passive area leads to Pt oxides formation and Pt dissolution in the passive area of the positive electrode (normally, the cathode), especially upon alternation of the OFF_N_2 sequence with the ON_C_Air sequence. **(c)** Illustrative scheme of H_2O_2 formation mechanism at the cathode in the shutdown procedure OFF_Air.

The OFF_Air procedure consists of simply closing the cathode inlet and outlet, leaving the cell in H_2/air open-circuit conditions. In that case, it is likely that H_2 crossover from the anode compartment induces formation of hydrogen peroxide H_2O_2 in the cathode, which should be detrimental to the PtNi/C cathode catalyst stability (in particular its carbon support) and its ORR efficiency [15]. Figure 12b illustrates that H_2O_2 (and then radicals) formation is expected at the cathode membrane/CL interface. Even if, the transition phase should be short, because of the natural consumption of the remaining O_2, Li et al.[59] reported that the permeability of H_2 through a PBI membrane doped with phosphoric is higher than in LT-PEMFC and is also increased by temperature. This stop mode also induces potential alternation of the whole cathode between the O_2 rich phase (*ca*. 1[13] V_{vsRHE}), to the H_2-rich phase (likely *ca*. 0-0.1 V_{vsRHE}), that could trigger Pt-O place exchange and PtNi dissolution, which is also detrimental to the PtNi/C catalyst stability.

The performances losses for the couple ON_C_Air/OFF_Air do not reveal large damages; it can be considered that both ON_C_Air and OFF_Air procedures are neither very degrading individually, nor combined, which suggests that the possible formation of hydrogen peroxide

during OFF_Air was not the main factor of degradations of the combined degradation tests ran in this study.

On the contrary, the couple ON_A_H_2/OFF_Air is by far the most degrading of the tested sequences (Figure 3). Although one cannot exclude that the problem of N_2 flushing that occurred during the ageing had an influence on the observed degradation, one can also easily understand that the startup procedure ON_A_H_2 is very degrading. The potential negative impact of ON_A_H_2 is obvious for the voltage losses observed at low current density, and the couple ON_A_H_2/OFF_N_2 induces also more damages than ON_C_Air/OFF_N_2. According to the literature[15], the ON_A_H_2 startup transition situation should lead to the presence of an active and a passive area of the cell upstream and downstream of the H_2 front, respectively. Parasite reactions, which can lead to accelerated degradation of the catalyst in the cathode (positive electrode) of the passive region, likely occur in the passive area of the cell. At variance with the processes commonly observed in the literature[53,60] when an H_2/air front exists at the negative electrode, here an H_2/N_2 is transiently present. Figure 12c presents the suggested reactions that possibly take place in the passive part considered as an "inverted cell". At the passive side of the cell negative electrode (normally the anode), the possible reduction reactions are the reduction of PtO, the reduction of phosphoric acid and of course capacitive reduction currents[60]. According to Prokop et al[55], the reduction of H_3PO_4 occurs following the equations described in figure 12c. Then as the potential difference between electrodes is imposed by the active part of the cell to a voltage close to 1 V, the positive electrode (normally the cathode) of the cell in the passive part should undergo oxidation reactions. The species available to be oxidized are the carbon support, Pt and phosphoric acid (reverse equations of the one described at the anode). The potential at which reduced phosphoric acid species can oxidize at the anode, according to literature[55] is around ca. 0.4V_{vsRHE}

(or below), which means that such oxidation reaction should be more favored than the oxidation of Pt, the latter happening at higher potential. Carbon corrosion is also an obvious possibility, together with phosphoric acid species oxidation; these two reactions should be the main degradation reactions observed during ON_A_H_2 in the passive region of the positive electrode. The context of the work does not allow to identify phosphoric acid doping level or species present in the electrode, then no conclusions could be given on the contribution of phosphoric acid reduction and oxidation in the degradation reaction in the passive area. Whatever this uncertainty, the large cathode carbon corrosion observed in the result section (CO_2 emission, cathode CL thickness decrease) is likely to be caused in a non-negligible way by the ON_A_H_2 procedure.

Besides the degradations observed at the cathode (positive electrode), the result section did also put forth that an important functionalization of the carbon support occurred at the anode, even though this electrode mostly operates at low potential throughout the test. In the literature[61–66], some authors report the impact of formation at low potential of phosphoric acid reduced species as H_3PO_3 or $H_3P_2O_6$ on the anode performances[55,67]. In particular, they explain that phosphoric acid, and its reduced form, are chemically linked by oxygen on Pt particles. One hypothesis that can be posited is therefore that the reduced phosphoric species produced at low potential (perhaps catalyzed by Pt) do interact with Pt, but also with the carbon support; the carbon functionalization and the related structure variation observed in XPS and Raman spectroscopy should therefore be explained by the formation of chemical C-O bonding between the carbon support and phosphoric acid reduced species. The impact of the reduced PA species described here agrees with the use of phosphoric acid to produce activated carbons[68,69]: below 400°C, the reaction of PA with carbon yields the formation of reduced species of phosphoric acid, that do activate the carbon at higher temperatures.

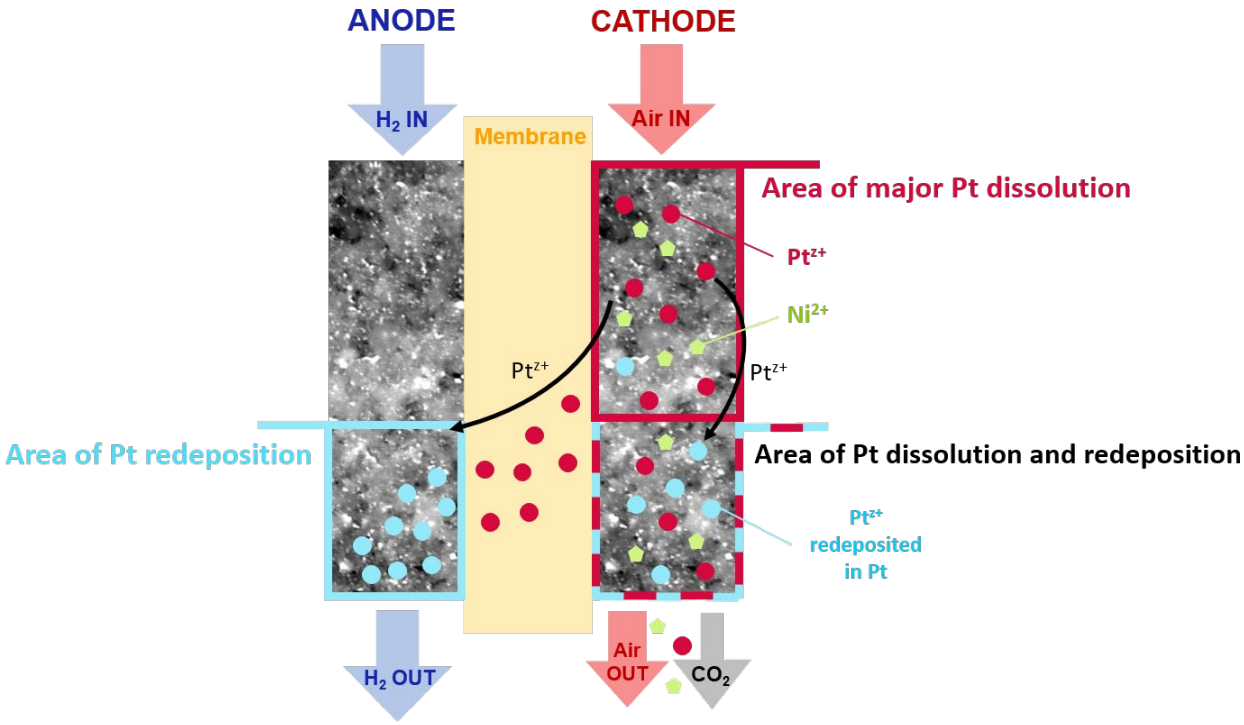

Figure 13. Illustrative scheme of Pt dissolution (mostly from the cathode inlet) and redeposition (mostly at the cathode and anode outlet), Ni leaching and carbon corrosion resulting from the combination of stationary and start-stop operation of the HT-PEMFC.

CONCLUSIONS

The present study reports catalyst degradation mechanisms identified in HT-PEMFC MEAs aged in al HT-PEMFC stack operated at 160°C for around 900 h, with deliberately applied startup/shutdown steps. After careful characterization of the MEA materials by complementary physicochemical and electrochemical techniques, well-known degradation mechanisms could be detected. PtNi nanoparticles growth, dissolution, migration, coalescence, and their detachment,

following the corrosion of the carbon support were observed at the cathode. All these degradations were induced firstly by the constant load operation between each start-up and shutdown, and also by the various procedures of start/stop tested here. The following degradation mechanism were identified:

- Cathode ECSA loss by Pt (and Ni) dissolution (Ostwald ripening mechanism) occurred during the constant operation and the ON_C_Air/ OFF_N_2 phases, leading to greatly decreased ORR (and thus cell) performances at the cell inlet. The metallic cations generated likely had important chemical interaction with PA and led to increased mass-transport losses (preventing dynamic reactant gases (O_2) and protons access to the catalytic sites).
- Cathode catalyst Ni leaching from the initial PtNi alloy in operation was found higher at the inlet of the cell, a region being more oxidant and acidic. The depreciated Ni content lowered the PtNi/C alloys performance for the ORR.
- Cathode carbon corrosion at the outlet of the cell was favored by the ON_A_H_2 startup procedure and (minorly) by formation of H_2O_2 in the OFF_Air procedure. It led to the formation of small agglomerates of NPs between carbon grains at the cathode.
- Anode outlet ECSA increase was explained by redeposition of Pt^{z+} species originating from the cathode degradation, after diffusion at OCV or migration in operation.
- Anode carbon functionalization was also observed, and explained by the chemical action of phosphoric acid and its reduced species at low potential, which was identified by Raman and XP Spectroscopy of the anode carbon support.

In this study, PA leaching could not be characterized by *in situ* or *post mortem* characterizations; however, it should participate in a non-negligible way to the degradations cited

before. Finally, the procedures identified as the more degrading are the ON_A_H_2 startup for carbon corrosion at the cathode (passive region), and the couple ON_C_Air/ OFF_N_2 for the formation of Pt^{z+} and their interaction with phosphoric acid. One could say that N_2 flush during these procedures is crucial to avoid larger degradations as observed for the ON_A_H_2/OFF_Air couple, although it does not at all prevent degradations.

CORRESPONDING AUTHORS

Axelle Baudy (Axelle.Baudy@grenoble-inp.fr) and Marian Chatenet (Marian.Chatenet@grenoble-inp.fr)

AUTHOR CONTRIBUTIONS

AB made the physicochemical and electrochemical characterizations of the MEA materials, and analyzed all the data and drafted the first version of the manuscript. MD made the MEA testing in HT-PEMFC and conceived the D/A procedures supervised by CT, JR and AJ. NS made the Raman spectroscopy experiments and helped in analyzing the data. GB made the XP spectroscopy experiments and helped in analyzing the data. FRD made the SEM and X-EDS observations and helped in analyzing the data. MS, LD and MC planed and conceived the study, and reviewed/completed the manuscript.

FUNDING SOURCE

The study was funded SAFRAN POWER UNITS in the frame of an ANRT funding scheme (CIFRE PhD).

ACKNOWLEDGMENT

The authors thank Vincent Martin for the ICP-MS measurements. Thierry Encinas and Stéphane Coindeau who performed XRD measurements, analyzed the results and help in the interpretation. Michel Mermoux for the analysis of Raman spectroscopy.

REFERENCES

1. Zhang, J. *et al.* High temperature PEM fuel cells. *J Power Sources* **160**, 872–891 (2006).

2. Ministère de la transition écologique et de la cohésion des territoires. Plan d'action ministériel sur les PFAS. *https://www.ecologie.gouv.fr/plan-daction-ministeriel-sur-pfas* (2023).

3. Araya, S. S. *et al.* A comprehensive review of PBI-based high temperature PEM fuel cells. *Int J Hydrogen Energy* **41**, 21310–21344 (2016).

4. Lee, K. S. *et al.* Phosphate adsorption and its effect on oxygen reduction reaction for PtxCoy alloy and Aucore-Ptshell electrocatalysts. *Electrochim Acta* **56**, 8802–8810 (2011).

5. Nart, F. C. & Iwasita, T. On the adsorption of H2PO4- and H3PO4 on platinum: an in situ FT-ir study. *Electrochim Acta* **37**, 385–391 (1992).

6. Galbiati, S., Baricci, A., Casalegno, A. & Marchesi, R. Degradation in phosphoric acid doped polymer fuel cells: A 6000 h parametric investigation. *Int J Hydrogen Energy* **38**, 6469–6480 (2013).

7. Kannan, A., Kabza, A. & Scholta, J. Long term testing of start-stop cycles on high temperature PEM fuel cell stack. *J Power Sources* **277**, 312–316 (2015).

8. Schonvogel, D., Rastedt, M., Wagner, P., Wark, M. & Dyck, A. Impact of Accelerated Stress Tests on High Temperature PEMFC Degradation. *Fuel Cells* **16**, 480–489 (2016).

9. Liu, G. *et al.* Studies of performance degradation of a high temperature PEMFC based on H3PO4-doped PBI. *J Power Sources* **162**, 547–552 (2006).

10. Modestov, A. D., Tarasevich, M. R., Filimonov, V. Y. & Zagudaeva, N. M. Degradation of high temperature MEA with PBI-H3PO4 membrane in a life test. *Electrochim Acta* **54**, 7121–7127 (2009).

11. Alegre, C. *et al.* Single cell induced starvation in a high temperature proton exchange membrane fuel cell stack. *Appl Energy* **250**, 1176–1189 (2019).

12. Chen, S., Gasteiger, H. A., Hayakawa, K., Tada, T. & Shao-Horn, Y. Platinum-Alloy Cathode Catalyst Degradation in Proton Exchange Membrane Fuel Cells: Nanometer-Scale Compositional and Morphological Changes. *J Electrochem Soc* **157**, A82 (2010).

13. Zhai, Y., Zhang, H., Liu, G., Hu, J. & Yi, B. Degradation Study on MEA in H3PO4/PBI High-Temperature PEMFC Life Test. *J Electrochem Soc* **154**, B72 (2007).

14. Dubau, L. *et al.* Heterogeneities of aging within a PEMFC MEA. in *Fuel Cells* vol. 12 188–198 (2012).

15. Dubau, L. *et al.* A review of PEM fuel cell durability: materials degradation, local heterogeneities of aging and possible mitigation strategies. *WIREs Energy and Environment* **3**, 540–560 (2014).

16. Alegre, C. *et al.* Post-mortem analysis of a 5-cell HT-PEMFC stack under the effect of induced starvation of reactant gases. in *Hyceltec Barcelona* (Barcelona, 2019).

17. Riasse, R. *et al.* Benchmarking proton exchange membrane fuel cell cathode catalyst at high current density: A comparison between the rotating disk electrode, the gas diffusion electrode and differential cell. *J Power Sources* **556**, (2023).

18. Dubau, L., Maillard, F., Chatenet, M., André, J. & Rossinot, E. Nanoscale compositional changes and modification of the surface reactivity of Pt3Co/C nanoparticles during proton-exchange membrane fuel cell operation. *Electrochim Acta* **56**, 776–783 (2010).

19. Van Der Vliet, D. F. *et al.* Unique electrochemical adsorption properties of Pt-skin surfaces. *Angewandte Chemie - International Edition* **51**, 3139–3142 (2012).

20. Maillard, F. *et al.* Size effects on reactivity of Pt nanoparticles in CO monolayer oxidation: The role of surface mobility. in *Faraday Discussions* vol. 125 357–377 (Royal Society of Chemistry, 2004).

21. Maillard, F. *et al.* Influence of particle agglomeration on the catalytic activity of carbon-supported Pt nanoparticles in CO monolayer oxidation. *Physical Chemistry Chemical Physics* 375–383 (2005) doi:10.1039/b411377b.

22. Maillard, F. *et al.* Effect of the structure of Pt-Ru/C particles on COad monolayer vibrational properties and electrooxidation kinetics. *Electrochim Acta* **53**, 811–822 (2007).

23. Authayanun, S., Im-orb, K. & Arpornwichanop, A. A review of the development of high temperature proton exchange membrane fuel cells. *Chinese Journal of Catalysis* **36**, 473–483 (2015).

24. Oono, Y., Sounai, A. & Hori, M. Long-term cell degradation mechanism in high-temperature proton exchange membrane fuel cells. *J Power Sources* **210**, 366–373 (2012).

25. Hu, J. *et al.* Performance degradation studies on PBI/H3PO4 high temperature PEMFC and one-dimensional numerical analysis. *Electrochim Acta* **52**, 394–401 (2006).

26. Prokop, M. *et al.* Degradation kinetics of Pt during high-temperature PEM fuel cell operation Part III: Voltage-dependent Pt degradation rate in single-cell experiments. *Electrochim Acta* **363**, 137165 (2020).

27. Santiago, E. I., Varanda, L. C. & Villullas, H. M. Carbon-supported Pt-Co catalysts prepared by a modified polyol process as cathodes for PEM fuel cells. *Journal of Physical Chemistry C* **111**, 3146–3151 (2007).

28. Travitsky, N. *et al.* Pt-, PtNi- and PtCo-supported catalysts for oxygen reduction in PEM fuel cells. *J Power Sources* **161**, 782–789 (2006).

29. Schenk, A. *et al.* Platinum-cobalt catalysts for the oxygen reduction reaction in high temperature proton exchange membrane fuel cells - Long term behavior under ex-situ and in-situ conditions. *J Power Sources* **266**, 313–322 (2014).

30. Malard, L. M., Pimenta, M. A., Dresselhaus, G. & Dresselhaus, M. S. Raman spectroscopy in graphene. *Phys Rep* **473**, 51–87 (2009).

31. Sadezky, A., Muckenhuber, H., Grothe, H., Niessner, R. & Pöschl, U. Raman microspectroscopy of soot and related carbonaceous materials: Spectral analysis and structural information. *Carbon N Y* **43**, 1731–1742 (2005).

32. Ferrari, A. C. & Robertson, J. *Interpretation of Raman Spectra of Disordered and Amorphous Carbon*. (2000).

33. Zhao, Z. *et al.* Carbon corrosion and platinum nanoparticles ripening under open circuit potential conditions. *J Power Sources* **230**, 236–243 (2013).

34. Hara, M. *et al.* Electrochemical and Raman spectroscopic evaluation of Pt/graphitized carbon black catalyst durability for the start/stop operating condition of polymer electrolyte fuel cells. *Electrochim Acta* **70**, 171–181 (2012).

35. Castanheira, L. *et al.* Carbon corrosion in proton-exchange membrane fuel cells: From model experiments to real-life operation in membrane electrode assemblies. *ACS Catal* **4**, 2258–2267 (2014).

36. Castanheira, L. *et al.* Carbon corrosion in proton-exchange membrane fuel cells: Effect of the carbon structure, the degradation protocol, and the gas atmosphere. *ACS Catal* **5**, 2184–2194 (2015).

37. DURAND Maël. Etude et optimisation des phases de démarrage et d'arrêt des piles à combustible de type PEM haute température en vue de maximiser leur durée de vie. (INPT, Toulouse, 2022).

38. Durst, J. *et al.* Degradation heterogeneities induced by repetitive start/stop events in proton exchange membrane fuel cell: Inlet vs. outlet and channel vs. land. *Appl Catal B* **138–139**, 416–426 (2013).

39. Iojoiu, C. *et al.* Membrane and Active Layer Degradation Following PEMFC Steady-State Operation. *J Electrochem Soc* **154**, B1115 (2007).

40. Guilminot, E., Corcella, A., Charlot, F., Maillard, F. & Chatenet, M. Detection of Pt[sup z+] Ions and Pt Nanoparticles Inside the Membrane of a Used PEMFC. *J Electrochem Soc* **154**, B96 (2007).

41. More, K., Borup, R. & Reeves, K. Identifying Contributing Degradation Phenomena in PEM Fuel Cell Membrane Electrode Assemblies Via Electron Microscopy. *ECS Trans* **3**, 717–733 (2006).

42. Touhami, S. *et al.* Anode aging in polymer electrolyte membrane fuel Cells I: Anode monitoring by ElectroChemical impedance spectroscopy. *J Power Sources* **481**, (2021).

43. Parry, V., Berthomé, G., Joud, J. C., Lemaire, O. & Franco, A. A. XPS investigations of the proton exchange membrane fuel cell active layers aging: Characterization of the mitigating role of an anodic CO contamination on cathode degradation. *J Power Sources* **196**, 2530–2538 (2011).

44. Puziy, A. M., Poddubnaya, O. I., Socha, R. P., Gurgul, J. & Wisniewski, M. XPS and NMR studies of phosphoric acid activated carbons. *Carbon N Y* **46**, 2113–2123 (2008).

45. Zhai, Y., Zhang, H., Xing, D. & Shao, Z. G. The stability of Pt/C catalyst in H3PO4/PBI PEMFC during high temperature life test. *J Power Sources* **164**, 126–133 (2007).

46. Guilminot, E. *et al.* Membrane and Active Layer Degradation upon PEMFC Steady-State Operation. *J Electrochem Soc* **154**, B1106 (2007).

47. M. Pourbaix. *Atlas of Electrochemical Equilibria in Aqueous Solutions*. (National Association of Corrosion Engineers, 1979).

48. Dubau, L. *et al.* Durability of Pt[sub 3]Co/C Cathodes in a 16 Cell PEMFC Stack: Macro/Microstructural Changes and Degradation Mechanisms. *J Electrochem Soc* **157**, B1887 (2010).

49. Takasu, Y. *et al.* Size effects of platinum particles on the electroreduction of oxygen. *Electrochim Acta* **41**, 2595–2600 (1996).

50. Watanabe, M., Sei, H. & Stonehart, P. The influence of platinum crystallite size on the electroreduction of oxygen. *J Electroanal Chem Interfacial Electrochem* **261**, 375–387 (1989).

51. Giordano, N. *et al.* Analysis of platinum particle size and oxygen reduction in phosphoric acid. *Electrochim Acta* **36**, 1979–1984 (1991).

52. GIORDANO, N. *et al.* Effect of platinum particle size on the performance of PAFC O2 reduction electrocatalysts. *Int J Hydrogen Energy* **19**, 165–168 (1994).

53. Reiser, C. A. *et al.* A Reverse-Current Decay Mechanism for Fuel Cells. *Electrochemical and Solid-State Letters* **8**, A273 (2005).

54. Lamibrac, A. *et al.* Experimental characterization of internal currents during the start-up of a proton exchange membrane fuel cell. *J Power Sources* **196**, 9451–9458 (2011).

55. Prokop, M., Bystron, T., Paidar, M. & Bouzek, K. H3PO3 electrochemical behaviour on a bulk Pt electrode: adsorption and oxidation kinetics. *Electrochim Acta* **212**, 465–472 (2016).

56. Prokop, M., Kodym, R., Bystron, T., Paidar, M. & Bouzek, K. Degradation kinetics of Pt during high-temperature PEM fuel cell operation part I: Kinetics of Pt surface oxidation and

dissolution in concentrated H3PO4 electrolyte at elevated temperatures. *Electrochim Acta* **313**, 352–366 (2019).

57. Cherevko, S., Topalov, A. A., Zeradjanin, A. R., Keeley, G. P. & Mayrhofer, K. J. J. Temperature-Dependent Dissolution of Polycrystalline Platinum in Sulfuric Acid Electrolyte. *Electrocatalysis* **5**, 235–240 (2014).

58. Durst, J., Chatenet, M. & Maillard, F. Impact of metal cations on the electrocatalytic properties of Pt/C nanoparticles at multiple phase interfaces. *Physical Chemistry Chemical Physics* **14**, 13000 (2012).

59. Li, Q., Jensen, J. O., Savinell, R. F. & Bjerrum, N. J. High temperature proton exchange membranes based on polybenzimidazoles for fuel cells. *Progress in Polymer Science (Oxford)* vol. 34 449–477 Preprint at https://doi.org/10.1016/j.progpolymsci.2008.12.003 (2009).

60. Maranzana, G., Moyne, C., Dillet, J., Didierjean, S. & Lottin, O. About internal currents during start-up in proton exchange membrane fuel cell. *J Power Sources* **195**, 5990–5995 (2010).

61. Gomes, B. F. *et al.* Following Adsorbed Intermediates on a Platinum Gas Diffusion Electrode in H3PO3-Containing Electrolytes Using in Situ X-ray Absorption Spectroscopy. *ACS Catal* **12**, 11472–11484 (2022).

62. Gomes, B. F. *et al.* Effect of phosphoric acid purity on the electrochemically active surface area of Pt-based electrodes. *Journal of Electroanalytical Chemistry* **918**, (2022).

63. Sugishima, N., Hinatsu, J. T. & Foulkes, F. R. Phosphorous Acid Impurities in Phosphoric Acid Fuel Cell Electrolytes: II . Effects on the Oxygen Reduction Reaction at Platinum Electrodes. *J Electrochem Soc* **141**, 3332–3335 (1994).

64. Sugishima, N., Hinatsu, J. T. & Foulkes, F. R. Phosphorous Acid Impurities in Phosphoric Acid Fuel Cell Electrolytes: I . Voltammetric Study of Impurity Formation. *J Electrochem Soc* **141**, 3325–3331 (1994).

65. Doh, W. H. *et al.* Scanning photoelectron microscopy study of the Pt/ phosphoric-acid-imbibed membrane interface under polarization. *ChemElectroChem* **1**, (2014).

66. Vogel, W. M. & Baris, J. M. Changes in the surface of platinum in hot concentrated phosphoric acid at low potentials. *Electrochim Acta* **23**, 463–466 (1978).

67. Orfanidi, A., Daletou, M. K., Sygellou, L. & Neophytides, S. G. The role of phosphoric acid in the anodic electrocatalytic layer in high temperature PEM fuel cells. *J Appl Electrochem* **43**, 1101–1116 (2013).

68. Neme, I., Gonfa, G. & Masi, C. Activated carbon from biomass precursors using phosphoric acid: A review. *Heliyon* vol. 8 Preprint at https://doi.org/10.1016/j.heliyon.2022.e11940 (2022).

69. Li, Y., Zhang, X., Yang, R., Li, G. & Hu, C. The role of H3PO4 in the preparation of activated carbon from NaOH-treated rice husk residue. *RSC Adv* **5**, 32626–32636 (2015).